This item is the archived peer-reviewed author-version of:

Bifunctional nickel-nitrogen-doped-carbon-supported copper electrocatalyst for CO_2 reduction

A Bifunctional Nickel-Nitrogen-doped-Carbon-Supported Copper Electrocatalyst for CO$_2$ Reduction

Daniel Choukroun, [§,*] Nick Daems, [§,‡] Thomas Kenis, [§] Tim Van Everbroeck, [†] Jonas Hereijgers, [§] Thomas Altantzis, [§] Sara Bals, [∥] Pegie Cool, [†] Tom Breugelmans, [§,‡,*]

[§] *Applied Electrochemistry and Catalysis (ELCAT), University of Antwerp, 2610 Wilrijk, Belgium*
[‡] *Separation & Conversion Technologies, Flemish Institute for Technological Research (VITO), 2400 Mol, Belgium*
[†] *Laboratory of Adsorption and Catalysis (LADCA), University of Antwerp, 2610 Wilrijk, Belgium*
[∥] *Electron Microscopy for Materials Research (EMAT), University of Antwerp, 2020 Antwerp, Belgium*

*Corresponding authors Daniel.Choukroun@uantwerpen.be; Tom.Breugelmans@uantwerpen.be

Abstract

Bifunctionality is a key feature of many industrial catalysts – supported metal clusters and particles in particular - and the development of such catalysts for the CO_2 reduction reaction (CO_2RR) to hydrocarbons and alcohols is gaining traction in light of recent advancements in the field. Carbon-supported Cu nanoparticles are suitable candidates for integration in state-of-the-art reaction interfaces, and here we propose, synthesize and evaluate a bifunctional Ni-N-doped-C-supported Cu electrocatalyst – in which the support possesses active sites for selective CO_2 conversion to CO, and Cu nanoparticles catalyze either the direct CO_2 or CO reduction to hydrocarbons. In this work, we introduce the scientific rationale behind the concept, its applicability and the challenges it holds from the catalyst's point of view. On the practical side, the deposition of Cu nanoparticles onto carbon black and Ni-N-C supports via an ammonia-driven deposition precipitation method is reported and explored in more detail using X-ray diffraction, thermogravimetric analysis and hydrogen temperature-programmed reduction. High-angle annular dark-field scanning transmission electron microscopy (HAADF-STEM) and energy-dispersive X-ray spectroscopy (EDXS) give further evidence of the presence of Cu-containing nanoparticles on the Ni-N-C supports, while revealing an additional relationship between the nanoparticle's composition and the electrode's electrocatalytic performance. Compared to the benchmark carbon-black-supported Cu catalysts, Ni-N-C-supported Cu delivers up to a 2-fold increase in partial C_2H_4 current density at -1.05V_{RHE} (C_1/C_2 =0.67) and a concomitant 10-fold increase of the CO partial current density. The enhanced ethylene production metrics, obtained by virtue of the higher intrinsic activity of the Ni-N-C support, point out towards synergistic action between the two catalytic functionalities.

1   Introduction

The development of energy-efficient catalysts for the electrochemical CO_2 reduction reaction (CO_2RR) to CO and C_2 products has reached several critical milestones lately, with metal-nitrogen doped carbons showing potential for industrial CO production by achieving reported H-cell current densities in excess of 6 A g^{-1} at overpotentials < 0.9V versus RHE (V_{RHE})[1-4]. Upscaling catalyst synthesis throughput and gas-liquid operation in CO_2 electrolyzers have pushed this metric beyond 100 mA/cm^2, due mainly to higher catalyst loadings and improved CO_2 mass-transfer[5-8]. From a mechanistic perspective, it is well known that the *CO adsorbate is a crucial intermediate in the direct conversion of CO_2 to CO on Ag, metal-nitrogen carbons and copper electrodes. Yet only on copper, a *CO intermediate or a desorbed $CO_{(g)}$ gas molecule can reduce directly to C_2 products such as ethylene[9], ethanol[10-12] and acetaldehyde, that all share the same - though disputable - reaction intermediate (*OCHCH$_2$[13-14]; *COCHO[15]). C-C coupling – the (pH independent) rate determining step - occurs via a *COH pathway on both Cu(111) and Cu(100) facets[15-16] and via CO dimerization on Cu(100) exclusively[9]. These pathways are favorable at low-moderate overpotentials and high pH that - along with optimized processing conditions in an alkaline electrolyzer - allow continuous electroreduction of CO_2 to ethylene at current densities > 100 mA cm^{-2} and potentials as low as -0.55V_{RHE}[17-18].

Such promising CO_2-to-ethylene conversion metrics have been obtained using seemingly simple reaction interfaces comprising gaseous CO_2, copper, carbon and hydroxide ions[18-19]. Most notably, Dinh et al[17] conceived an abrupt reaction interface consisting of a sputtered nanometer-sized metallic Cu layer, sandwiched between an additional layer of carbon black and a Teflon membrane. Faradaic efficiencies of 70% and continuous operation lasting 150 hours in 7M KOH (~30wt.%) were achieved, albeit with a low single-pass conversion[20]. The authors attributed the enhanced stability of the new electrode configuration to the presence of the carbon black layer that improves both the long-term mechanical and electrical connectivity of the catalyst layer. Moreover, the carbon black layer was claimed to improve the current distribution in the electrode, while maintaining a negligible contribution to the total current

density. However, we took the approach that metal-nitrogen-doped carbons in general and Ni-N-doped carbons in particular, can contribute both actively and selectively to the total current density, by acting as co-catalysts or CO suppliers to Cu.

The choice of carbon in the aforementioned studies and in our work comes as no surprise. For example, electrodes consisting of copper NPs in contact with onion-like carbon NPs exhibited increased stability and faradaic efficiency towards ethylene[21]. This improvement in C_2 selectivity stemmed in part from the higher selectivity of the support itself towards carbon monoxide, and an increase in surface CO concentration. In analogy to a Cu-carbon interface, one could reason that the best CO producing metal catalysts, Au, Ag and Zn, could increase the C_2 selectivity of neighboring Cu ensembles in the same manner. Recent literature on sequential/tandem catalysis on Cu_xZn[11], Au/Ag-Cu microarrays[22] and Ag-Cu nanodimers[23] reinforced this line of reasoning while demonstrating at the same time that the transport of CO from one active site to another can occur both on the range of several nanometers as well as several microns[22] - within the hydrodynamic boundary layer. Like Au and Ag, nitrogen-doped carbons are excellent CO producing catalysts, but examples of nitrogen-doped supported Cu are scarce[24]. Moreover, although nitrogen-doped carbons form CO as selectively as metal-nitrogen-doped carbons do, they do so in a limited and relatively positive potential interval[5]. Among the metal-nitrogen-doped carbons, it has been shown that Ni-N-C has the highest intrinsic activity and selectivity[2]. We also noted that at $-0.6V_{RHE}$, the adsorption of *H on Ni-N-C is unfavorable[2] and that in addition, the maximum *CO coverage on Cu is detected in the same potential interval as CO evolution on Ni-N-C[17], depending on the electrolyte concentration and cell configuration (See also Figure S.1 of the Supporting Information). Theoretical studies have shown further that *CO coverage weakens the adsorption energies of *H on various metals[25], including Cu. In the boundary layer region between the doped-carbon surface (containing Ni-N_x sites)[2, 26] and Cu NPs, it was hypothesized that a favorable environment for short-distance CO diffusional transport between active sites could be sustained.

In order to form the desired Cu-carbon interface, we synthesized a Ni-N-C support onto which we deposited copper nanoparticles by means of an ammonia-driven deposition precipitation method (ADP).

4

The ADP method has already been applied in our laboratories for the synthesis of platinum-group-metals-free automotive catalysts, based on well-dispersed CuO nanoparticles on a SBA-15 support. The improved stability of these catalysts was explained by the strong metal-support interaction, which limits particle mobility under the harsh conditions encountered in the exhaust outlet gas[27-28]. It was rationalized that such a method could also produce stable Cu nanoparticles on carbon, and that the particles will be more resistant to agglomeration during the course of synthesis or electrolysis[29-31]. Despite the fact that the nature of carbon support deviates strongly from that of silica supports[31], the ADP method proved successful - even after a thermal reduction treatment at 600°C - in the synthesis of Cu nanoparticles in the size range 25-50nm. This moderate particle size window is important because particles < 15 nm tend to have more undercoordinated Cu atoms, stronger bonding to *H and hence, higher activity towards the hydrogen evolution reaction (HER)[32]. On the other hand, larger particles have lower mass-based activity, accompanied by higher CH_4/C_2H_4 (C_1/C_2) ratios[32-33].

In what follows, we focus on the synthesis of the bifunctional Cu-Ni-N-C catalyst and its evaluation in at high overpotentials in which both functionalities coincide, i.e. at $E < -0.9V_{RHE}$. Compared to the benchmark carbon-black supported Cu catalysts, Cu-Ni-N-C delivers a 2-fold increase in partial C_2H_4 current density at $-1.05V_{RHE}$ and $-1.1V_{RHE}$ ($C_1/C_2 = 0.5-0.67$) and a concomitant elevated CO partial current density. As will be discussed in the following sections, these results have been obtained because of the high intrinsic activity of the Ni-N-C-support, the proximity of Cu to Ni-N$_x$ or N-doped active sites and the particles' distribution on the support – a merit of the ADP method.

2 Experimental Section

Synthesis

Three conductive carbon black and active carbon powders were selected as benchmark support materials: Vulcan XC72 (VC), ENSACO®-350G (EC) and Norit® SX1G activated carbon (AC). Nickel-nitrogen-doped carbons (Ni-N-C) were prepared from EC and AC using the procedures described by Daems et al [34-35]. The method relies on the pyrolysis of Ni-containing polyaniline-C composites, having a 1:1 nitrogen-to-nickel atomic ratio, at 900°C. Copper nanoparticles were deposited onto carbon black and Ni-N-C by means of an ammonia-driven deposition precipitation method in aqueous media. Copper loaded samples were dried, calcined under air and then reduced thermally in 5% H_2/Ar to obtain the final catalyst. A more detailed description of the synthesis procedures and physicochemical properties can be found in the Electronic Supporting Information (ESI†, Section S2-S3).

Physico-chemical characterization

The impregnated carbon powders were analyzed for their copper, nickel content and calcination temperature in air using a Q500 thermogravimetric analyzer (TA Instruments). The temperature of the furnace was ramped from 40°C to 600°C-800°C at 5°C/min. Platinum pans were used in all measurements. The Cu and Ni wt.% was calculated from the residue at 600°C, assuming complete oxidation of Cu to CuO and Ni to NiO. The leachable Ni content of selected materials was analyzed using an Agilent 7500 Series ICP-MS. A 10mg aliquot was digested in *aqua regia* at 70°C overnight and then diluted to the appropriate concentration range (10-300 ppb).

Scanning electron microscopy measurements were performed on a Thermo Fischer Scientific Quanta FEG 250 microscope, operated at an acceleration voltage of 5kV. Samples suitable for Scanning Transmission Electron Microscopy (STEM) observations were prepared in Ar atmosphere in the glovebox, by drop-casting the sample solution onto a C-coated Mo TEM grid. The grid was mounted in a Gatan model 648 double tilt vacuum transfer holder, in order to avoid contact with air during the

transfer of the sample into the TEM. High Angle Annular Dark Field STEM (HAADF-STEM) images, STEM Energy Dispersive X-ray Spectroscopy (STEM–EDXS) and STEM Electron Energy Loss Spectroscopy (STEM-EELS) maps were acquired using an aberration corrected Thermo Fischer Scientific Titan electron microscope and a Thermo Fischer Scientific Osiris electron microscope, both operated at 200kV and equipped with the ChemiSTEM system36[36].

X-ray diffraction experiments were performed on a Huber X-ray diffractometer equipped with a G670 Guinier camera (Huber GmbH&Co, Germany) using the Cu Kα1 radiation (λ=1.5405981Å). Temperature programmed reduction (TPR) measurements of the catalysts were performed on a Quantachrome iQ instrument. Prior to the measurement, ~20 mg of the sample was degassed at 200°C for 16 h. After cooling, the sample was first pretreated at 250°C under a Helium flow for 1 h. Subsequently, the sample was reduced with 5% H_2/Ar at a flow rate of 25 sccm and the temperature was ramped from 100°C to 800°C with a heating rate of 10°C min^{-1}. The hydrogen consumption was continuously monitored using a thermal conductivity detector (TCD). The final TCD signal was normalized by the catalyst weight determined after degassing and prior to the measurement.

Electrochemical measurements

Electrochemical measurements were performed using a potentiostat/galvanostat system (PARSTAT4000, Ametek® Princeton Applied Research). Experiments were conducted in an H-type cell equipped with a homemade cylindrical cathodic chamber (Figure S.8) connected to an in-line gas chromatograph (Trace1300, Thermo Fischer Scientific). Anode and cathode were separated by a Nafion® 117 cation exchange membrane. On the anode side, a rectangular Pt plate (0.5cm^2, Meinsberg GmbH) was used as counter electrode. The reference electrode was a 4-mm Ag/AgCl (3M KCl, +0.210V vs. SHE, Metrohm). The cathodic chamber filled with 2.5 cm^3 0.1M $KHCO_3$ (pH 6.7) was purged continuously with 1 sccm CO_2 using a mass flow controller (GF-080, Brooks Instruments). Electrochemical Impedance Spectroscopy (EIS) measurements were conducted before the experiments on the blank glassy carbon electrodes in order to determine the uncompensated resistance R_u. Frequencies ranging from 20 kHz to 1 Hz were scanned and the amplitude of the sinusoidal perturbation

was set to 10 mV. The potential was corrected actively for 85% of the determined value, and additional correction was performed after the measurement.

Electrochemical active surface areas (ECSA) were measured after the electrolysis protocol by conducting multiple cyclic voltammetry experiments in an Ar-purged 0.1M $HClO_4$ solution. Capacitive current densities (j_c) were recorded in a suitable interval during 10 cycles at scan rates (v) of 20, 50, 75, 100 and 125 mV/s.

All potentials are reported versus the reversible hydrogen electrode (RHE), unless stated otherwise.

Electrode Preparation

Glassy carbon (GC) electrodes were polished with alumina suspensions (Struers) and rinsed with milli-Q water (18.2 MΩ cm, Synergy Merck) before use. To prepare the catalyst ink for deposition, Cu/C suspensions containing 1.5-2.0 mg_{Cu}/ml were ultrasonicated in 1ml of isopropanol using a 0.3 cm axial probe and a 35 kHz ultrasonic transducer (Lab120, SinapTec). A Nafion® perfluorinated resin solution was employed as binder material. The active material-to-binder ratio of the dried coating was 90:10, and the molar Nafion/Cu ratio was ~9%, based on a binder equivalent weight (EW) of 1100 g/mol monomer. 6-10µl of Cu/C suspension were drop-casted stepwise on the glassy carbon substrate to obtain a copper loading of 20-30 µg cm^{-2} and a total catalyst loading of 0.345 mg cm^{-2}.

Gaseous and Liquid Product analysis

Gaseous products were separated using a micropacked column (ShinCarbon ST 100/120, 2 m, 1 mm ID, Restek) and detected by means of a thermal conductivity detector (TCD) operating at 200°C. Samples were injected automatically into the column from the reactor's outlet. The total duration of the analysis was 11 minutes. Helium was used as carrier gas with a column flow rate of 10 ml/min.

Formic acid was analyzed by means of high-performance liquid chromatography. An Alliance 2695 apparatus (Waters) equipped with a photodiode array detector (PDA) at 210nm and an IC-pack ion

exclusion column (7µm, 7.8x300 mm, Waters) were used. The mobile phase was a 0.1% $HClO_4$ in milli-Q water mobile phase flowing at 1 ml min^{-1}.

3   Results and discussion

3.1   Deposition of Cu NPs onto Ni-N-C via Ammonia-driven deposition precipitation

Ammonia-driven Deposition Precipitation ADP is presented in this section as an enabling method for the deposition of copper nanoparticles onto various carbon supports, including Ni-N-doped carbons. The method relies primarily on the electrostatic adsorption of positively charged $[Cu(NH_3)_n(H_2O)_{6-n}]^{2+}$ complexes onto a negatively charged surface at a pH higher than the point of zero charge (PZC) of the support material, a step that precedes cation exchange with the support in solution[37-38]. On SiO_2, it is known that copper-ammonia complexes remain in electrostatic interaction with the surface as long as the sample is wet, and that drying brings upon the formation of grafted Cu-O[28, 37]. It was hypothesized that a similar mechanism may take place on carbon, where adsorption of Cu ions or complexes to carboxyl or ionized O$^-$ functional groups is expected[31]. By consequence, a lower PZC of the support material should enable a stronger electrostatic interaction between the copper-ammonia complexes and dissociated surface moieties. Dynamic light scattering experiments provided us with the insight that both EC and VC carbon blacks have a strong and negative zeta potential at the pH of interest for electrostatic adsorption (Figure S.3, ESI†). Thermogravimetric analysis proved that adsorption of copper at loadings < 9 wt.% could be obtained irrespective of the surface loading and acid treatment on EC and VC. The measured pH shift after 48h of contacting varied only between -0.07 and -0.17 pH units for EC and VC, respectively. These values indicated that electrostatic adsorption was conducted well above the PZC of the support, as expected from the zeta potential measurements. It is important to mention that Cu loadings < 9 wt.% were chosen as a compromise between the desired particle size range (20-50nm) and the maximum obtainable loading (for a single deposition). This choice of loading was rationalized by

an initial SEM screening of reduced samples and later justified by employing HAADF-STEM imaging and STEM-EDXS on the calcined and reduced samples, as discussed in the following paragraphs.

Calcination The proper conditions for calcination of the Cu-loaded carbon support were determined based on a thermogravimetric analysis of the dried Cu-loaded samples. Degradation of the support can occur at temperatures as low as 400°C under oxidative conditions, as can be deduced from Figure 1a, where the differential weight loss with respect to temperature is depicted.
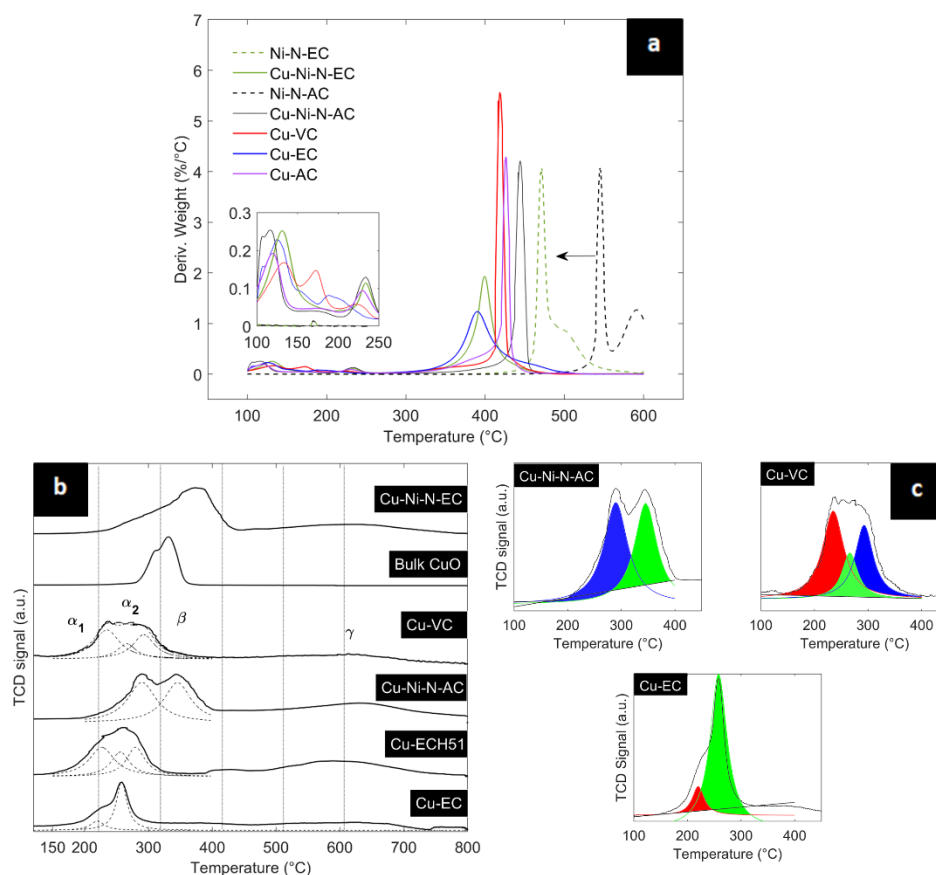

Figure 1 (a) Thermogravimetric analysis of Ni-N-C and carbon-black supported Cu. (b) Normalized H_2-TPR profiles of calcined carbon supported copper samples. (c) H_2-TPR peak deconvolution (Section S3.2, ESI†).

The differential thermal gravimetric (DTG) plots of Cu-EC, Cu-VC, Cu-AC, Cu-Ni-N-AC and Cu-Ni-N-EC exhibit a major peak at 390.9°C, 418.6°C, 426.8°C, 444.1°C and 398.8°C, respectively. The DTG curves of Ni-N-AC/EC have the same pattern, namely a sharp decomposition peak at lower temperatures and a shoulder/broader peak at higher temperatures. The sharp decomposition peak of Ni-N-AC/EC is attributed to the presence of residual non-graphitized polyaniline in the sample, as the degree of

10

graphitization is influenced by the extent of nitrogen and nickel[39] doping. It is also observed that this peak shifts to lower temperatures depending on the carbon precursor, with carbon black preceding active carbon. After ADP, the pattern changes and a single peak emerges at lower temperatures, indicating the adsorption of Cu. From the left hand side of Figure 1a, one can identify 2-3 peaks between 100°C and 250°C. These peaks correspond primarily to decomposition of the nitrate salt and/or $Cu(OH)_2$, elimination of NH_3[27, 37] and oxidation of functional groups on the carbon support itself[40-41]. Whereas the low-temperature peaks are assigned to $Cu(NO_3)_2.3H_2O$ melting and NH_3 elimination, peaks at temperatures between 200°C-250°C are allocated to the decomposition of $Cu(NO_3)_2.3H_2O$ or $Cu(OH)_2$ to CuO[42-43]. It is noticeable that the latter peak is more pronounced in the case of Cu-Ni-N-AC and Cu-Ni-N-EC, and this is associated with a saturation of the surface with ion-exchanged copper, leading to the formation of two particle-size populations.

Characterization by H_2-TPR and HAADF-STEM hydrogen temperature-programmed reduction (H_2-TPR) allows assessment of the dispersion, state and reduction temperature of the carbon supported CuO phase after the calcination step. There is a long-standing literature on supported copper heterogeneous catalysts that have been characterized using this method, with the majority of the studies conducted on Cu/SiO_2 systems. In these systems, the reduction onset temperature and hydrogen consumption peak during Cu^{2+}/CuO reduction depend on the experimental conditions: cell configuration, heating rate, pretreatment, hydrogen partial pressure, porosity and the water vapor pressure in the gas stream[44-45]. As a result, reported hydrogen consumption temperatures often deviate, even between comparable copper catalysts. Nevertheless, there is a broad consensus in literature on the fact that small CuO particles (~2-8 nm) undergo reduction at low temperatures (150-200°C) [45-47], and at lower temperatures than bulk CuO[48-50]. In contrast to this observation, relatively higher reduction temperatures (200-300°C) have been associated with the interaction of Cu^{2+} or CuO with the support, as in the case of stabilization of CuO by aminopropyl groups[47], copper phyllosilicates[50] and grafted Cu-O-Si species[28]. Considering the possible CuO/Cu^{2+} species and their somewhat different interaction with the support, hydrogen consumption can be convoluted over a broad temperature range between 200°C and 350°C[47, 51-52]. The H_2-TPR profiles of selected calcined carbon-supported samples from this study (Figure 1b-c) display

peaks in the same temperature interval. For example, the reduction peak α_1 or α_2/β of Cu-VC appearing at a temperature of 235°C and 258-266°C can be assigned to the presence of well-dispersed CuO particles on the support material, differing only in their interaction with the support[28].

In the case of calcined Cu-Ni-N-AC, the attribution of the β peak to the presence of small CuO nanoparticles is complemented by HAADF-STEM and STEM-EDXS analyses of the sample (Figure 2a-b), showing clusters of Cu-containing particles with a size range of 5-40 nm. By contrast, the second reduction peak at 375°C appears at a higher temperature compared to the carbon-black supported samples, in a region that coincides with the reduction of bulk CuO. This feature predicts the presence of larger CuO crystallites on the calcined Cu-Ni-N-AC sample (shown in Figure S.4, ESI†), that may originate from precipitation of $Cu(OH)_2$ in the bulk solution during ADP or $Cu(NO_3)_2$ decomposition during calcination. Nevertheless, Figure S.5 and Figure S.6d of the Supporting Information show homogeneous areas in the reduced Cu-Ni-N-EC and Cu-Ni-N-AC samples, respectively, where Cu particle size is comparable to that of Cu-EC and Cu-VC (Table 1).

Thermal Reduction The presence of metallic copper after thermal reduction and CuO after calcination was first confirmed by calculating the lattice parameter from XRD data (Figure 2c and 2d, respectively). The main peaks corresponding with face-centered-cubic Cu(111), (200), (220) and (311) crystallographic planes were identified at 43.28°, 50.42°, 74.14°, 89.94°. It is important to mention that Cu-VC, Cu-EC and Cu-Ni-N-AC samples that were stored under argon and exposed to air briefly before the measurement did not show a diffraction peak for Cu_2O (at $2\theta=36.4°$). As an approximation, we have therefore modelled the particles as pure metallic spheres and estimated their diameter from the peak broadening using the full-width at half-maximum (fwhm) of a given Bragg reflection and a slightly modified version of the Scherrer formula, after the work of Nanda[53-54] and Borchert[55] (Eqn. S.11, ESI†). Particle diameters were calculated independently for each diffraction peak and the resulting average is given in Table 1, together with an overview of Cu and Ni loading, Cu/Ni ratio, particle size estimated from SEM images and corresponding surface areas. While XRD and SEM remain very useful techniques for routine analysis and screening of carbon-supported Cu catalysts, they do not provide sufficient

12

resolution with respect to features smaller than 5 nm (e.g. small metallic clusters, Ni and N doping), nor can they tell the proximity of such sites to metallic Cu particles – a core aspect of the bifunctional catalyst design. Therefore, a combination of high-resolution HAADF-STEM imaging, STEM-EDXS and STEM electron energy loss spectroscopy (STEM-EELS) analysis was used to further characterize the thermally reduced Cu-Ni-N-AC. These additional data are provided in Figure S.7 of the supporting information.
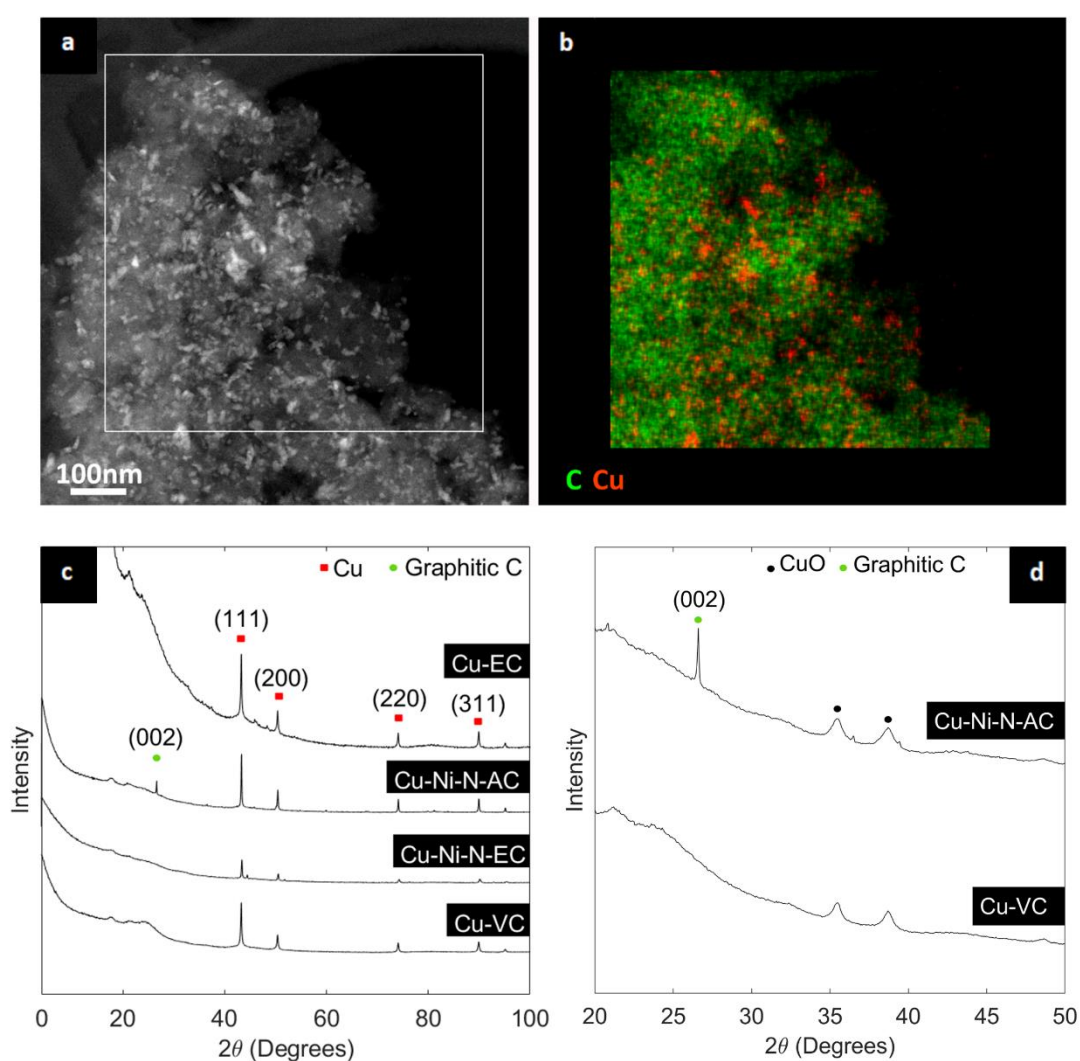

Figure 2 HAADF-STEM image and the corresponding STEM-EDXS elemental maps of the calcined Cu-Ni-N-AC sample (a,b). X-ray diffractograms of reduced (c) and selected calcined carbon-supported samples (d).

Table 1 Characterization of Cu-C powders. Weight loadings, mean XRD-based particle size and average diameters based on SEM

	Cu Wt. %[‡]	Ni Wt.%[‡]	Ni wt.%[§]	Cu/Ni (wt.%)	XRD-based particle size (nm)				XRD-based Surface area ($m^2 g^{-1}$)	SEM average diameter (nm)
					(111)	(200)	(220)	Avg.		
Cu-EC	8.18	-	0.18	-	42	31	14	29±14	23	45±14
Cu-VC	7.59	-	n.d.	-	47	48	30	42±10	16	49±15
Cu-AC	9.59	-	0.15	-	78	42	57	59±20	11	-
Cu-Ni-N-AC	5.49	4.42	0.29	1.2	71	65	75	70±5	10	36±10[*]
Cu-Ni-N-EC	5.36	4.91	2.18	1.1	54	42	47	47±6	20	36±10

* from Figure S.6d
‡ Residue (TGA)
§ Leachable Ni content (ICP-MS).

To conclude this section, we have shown that the ADP method succeeds in forming well-dispersed CuO (after calcination) and metallic Cu particles (after thermal reduction) on two common carbon black supports, active carbon and on the novel Ni-N-AC and Ni-N-EC supports. The first adsorption and drying steps as well as the metal loading in solution are crucial for obtaining a unimodal particle-size distribution. Using STEM-EDXS we have been able to attribute the low temperature H_2-TPR peaks to the presence of clusters of Cu-containing particles with a size range of 5-40nm. We point out that reduction at 600°C can be conducted without severe agglomeration of the nanoparticles, while ensuring quantitative reduction of Cu^{2+} and Cu^{1+} species to Cu°. That being said, the hydrocarbon selectivity of supported Cu NPs in this study is governed not only by size[56] or particle distribution on the support[57-59]. It will be shown that the particle's composition and the local electrode conditions are strongly affected by the use of Ni-N-C as support, with both negative and positive consequences for the overall CO_2RR activity of the electrodes.

3.2 Electrochemical Results

3.2.1 Setup evaluation and performance of carbon supports

First, the activity of glassy carbon substrates was evaluated by means of linear sweep voltammetry (LSV) between $-0.35V_{RHE}$ and $-1.2V_{RHE}$ in CO_2-saturated 0.1M $KHCO_3$. Under steady state conditions at -1.1 V_{RHE}, the current density of the electrodes dropped to less than -0.5 mA cm_{geo}^{-2}, with the concentration of hydrogen and CO falling below than the limit of quantification (~0.1v% for H_2, ~0.05v% for CO, CH_4). Similar LSV experiments gave a first indication of the CO_2RR and HER activity of blank EC, VC and AC carbon supports (Figure S.9, ESI†). Chronoamperometric measurements at potentials lower or equal to $-1.1V_{RHE}$ combined with gas and liquid product analysis revealed that EC and VC supports produce carbon monoxide and formate with a maximum total CO_2RR selectivity of 35% (blank EC), yet at low current densities (Table S.3, ESI†). In contrast, Ni-N-AC and Ni-N-EC supports that were studied under the same conditions produced CO at high current densities while their faradaic efficiencies to CO were in excess of 94% at $-0.8V_{RHE}$ (Figure 3a-b) - matching state-of-the-art results in an H-cell configuration[1-2, 26, 5, 60] (Table S.8, ESI†). For instance, the Ni-N-EC support generated a maximal CO partial current density of -4.6 mA/cm$_{geo}^2$ at $-0.9V_{RHE}$ and a loading of 0.345 mg cm^{-2} (13.4 A g^{-1}), corresponding to an areal turnover frequency of 0.083 mol CO mol Ni^{-1} s^{-1} (Section S.5.2, ESI†). With respect to their ECSA (Table S.3 and Figure S.10, ESI†), CO partial current densities of Ni-N-EC are up an order of magnitude compared to Cu-EC (Figure 3c). These results clearly demonstrate the superior performance of the Ni-N-doped carbons compared to the carbon and Cu-loaded carbon benchmarks.

Based on this performance, we also arrived at the conclusion that metallic impurity levels in the electrolyte and cell (e.g. Ni and Pt) were insignificant, and this finding was further consolidated by an ICP-MS analysis of the electrolyte solution (S.5.5, ESI†). Regarding the employed cell design, it could have been expected that the lack of convection in the cell - which translates in a thicker hydrodynamic boundary layer[61] (calculated value = 180 µm, S5.6., ESI†) – would lead to CO_2 depletion in the boundary

layer. Furthermore, the relatively large CO_2 bubble size (1.0mm capillary) could have led under certain conditions to CO_2 undersaturation in the cell[62]. Although the CO selectivity maxima of blank Ni-N-AC and Ni-N-EC point otherwise, increasing the partial pressure of CO_2 in the system does seem to lead to lower current densities and suppression of HER at high overpotentials (Figure 3d). At lower applied potentials and currents, it is the relatively low Ni-N-AC and Ni-N-EC loading (0.345 mg cm^{-2}) and applied currents, as well as the moderate S/V ratio (0.11 cm^{-1}) of the cell, that explain the negligible influence of cell design on CO_2RR activity and selectivity.
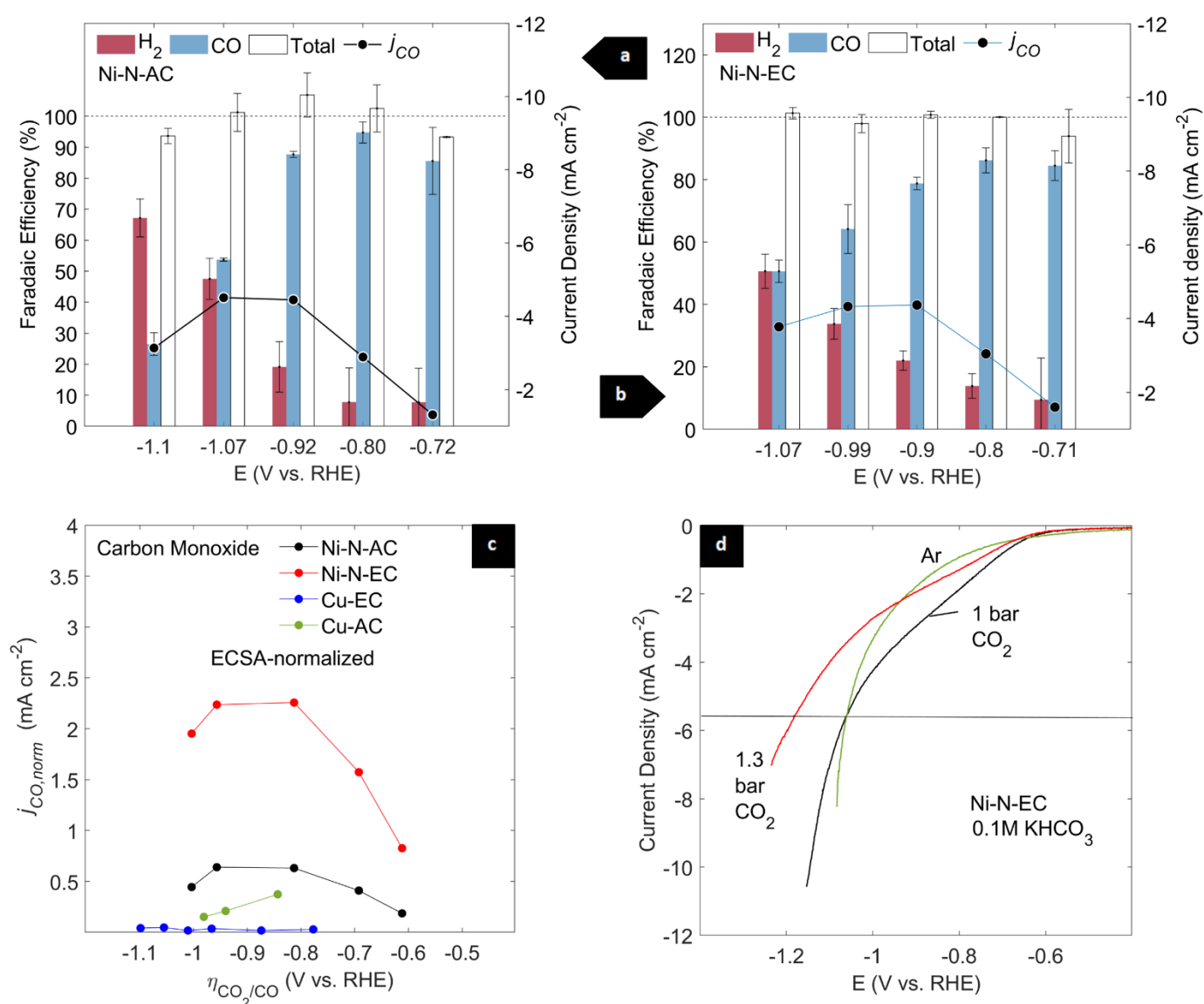

Figure 3 (a) Product distribution and CO partial current density of Ni-N-AC as a function of potential (b) Product distribution and CO partial current density of Ni-N-EC as a function of potential. (c) Comparison of partial current densities as a function of the overpotential $\eta CO_2/CO$. (d) LSV of Ni-N-EC under various processing conditions. All experiments were conducted in 0.1M KHCO$_3$ at 18ºC, 1 sccm CO$_2$.

3.2.2   Performance of Carbon-supported Cu Catalysts

According to literature[62], CO_2 reduction at high overpotentials and current densities may result in undersaturation of the electrolyte and an elevated H_2/CH_4 product ratio. The observed electrochemical performance of carbon-black-supported Cu NPs suggests that under the employed conditions in this study – such effect is taking place. Whereas in the work of Baturina et al[33] one observes relatively low hydrogen faradaic efficiencies ($\leq 20\%$) for 20 wt.% Cu/VC at $|E| > 2.0V$, and a plateau in CH_4 and C_2H_4 evolution, we noticed a maximum in hydrocarbon selectivity at $-1.15V_{RHE}$ followed by a FE decrease at higher overpotentials. The reason for the discrepancy between the studies is two-fold: on the one hand, the enhanced convection in the former case - achieved by the use of a rotating-disk working electrode operating at 1600rpm - reduces the thickness of the hydrodynamic boundary layer[61] and improves CO_2RR selectivity due to an increased local CO_2 concentration. Of course, it is now known that the effect of convection on CO_2RR selectivity could be reproduced by different ways, for example by the use of cationic surfactants[63], or by manipulation of the local pH and stabilization of key reaction intermediates, which are brought about by addition of Cs^+ to the electrolyte[64-65]. On the other hand, the lower copper loading of the studied samples in this work (~8 wt. %, Table 1) translates into a higher share of exposed support material for the same gravimetric electrode loading and this excess support material contributes negatively to the selectivity at higher overpotentials.

Figure 4 depicts our experimental findings and the complete product distribution on VC (Figure 4a) and EC-supported Cu NPs (Figure 4c) in the interval $[-1.2, -0.9]V_{RHE}$. Both materials show a similar selectivity trend – namely overlapping potential intervals in which the selectivity is dominated by formate, CO, ethylene and finally methane in the order of increasing overpotential - in accordance with the trend observed by Hori et al[66] and more recently by Kuhl et al[67]. The fact that the selectivity of both methane and ethylene drops at higher overpotentials and current densities, while that of H_2 increases is in line with the CO_2 undersaturation hypothesis. Moreover, the C_1/C_2 ratios (Figure 4d), 1.5 ± 0.4 and 1.4 ± 0.5 for Cu-VC and Cu-EC respectively, favored methane at potentials negative and equal to $-1.1V_{RHE}$. This points out to a general agreement with the model that was proposed by Reske et al, in which hydrocarbon selectivity (dominated by CH_4) rises quasi linearly with particle size between 15nm

and 50nm[32, 56]. In addition, we can conclude that the C_1/C_2 ratio is independent of the carbon black carrier. This observation is supported by both the minor differences in ECSA-normalized activity between Cu-loaded EC, VC and AC and their blanks (Table S.4 and Table S.3, ESI), and by the general agreement in Cu particle size of the catalysts after ADP (Table 1).
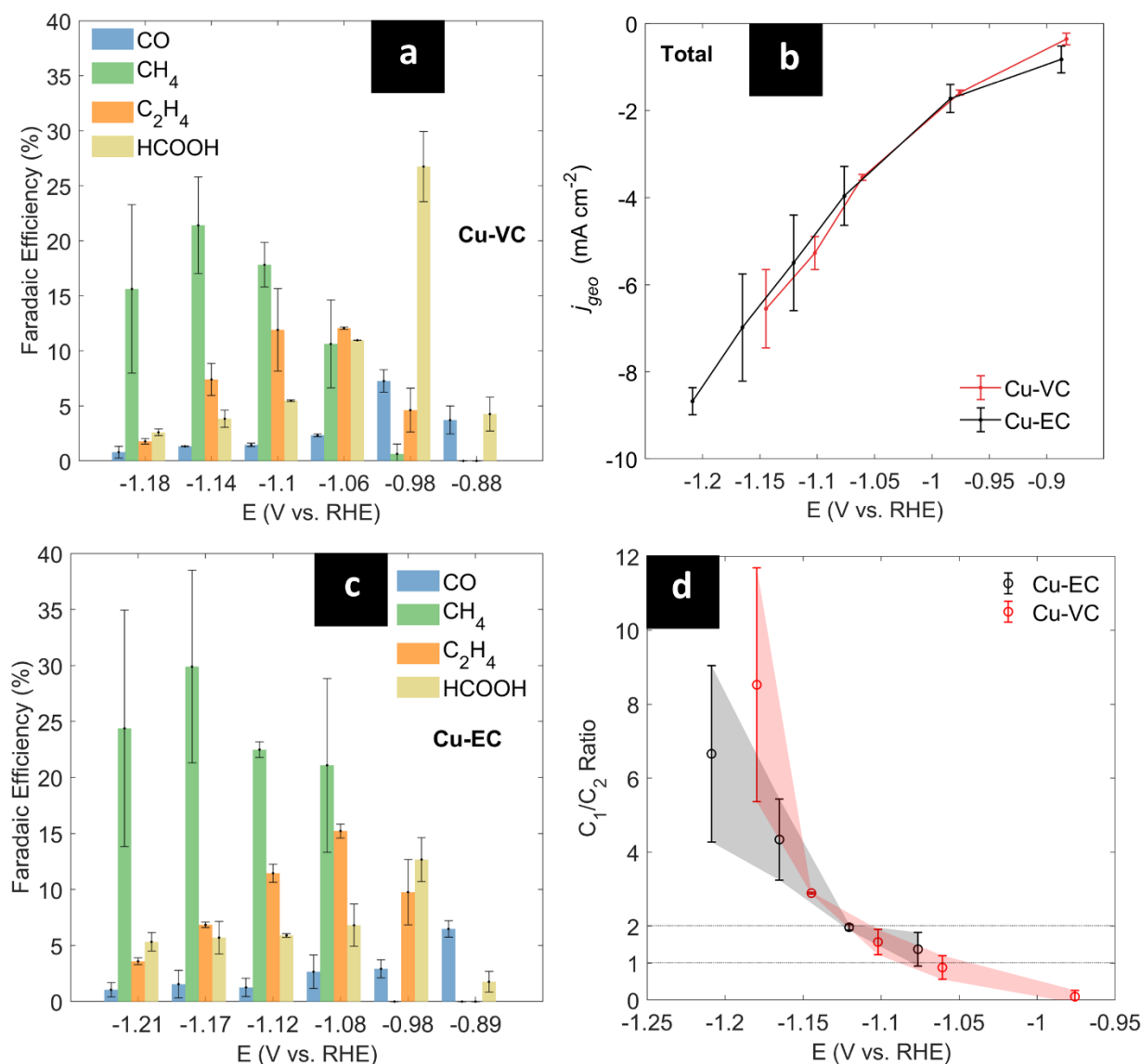

Figure 4 Product distribution as a function of potential for Cu-VC (a), Cu-EC (c). Steady-state j-E comparison between Cu-VC and Cu-EC (b) and C1/C2 ratio as a function of potential (d).

The comparably high geometric partial CO current densities of Ni-N-EC and Ni-N-AC that were presented in Figure 3a and 3b painted an optimistic picture regarding the CO_2 reduction performance of Cu-Ni-N-AC and Cu-Ni-N-EC. Indeed, in the case of Cu-Ni-N-AC, improvement was measurable (Figure 5 and Table S.4), especially with respect to CO and C_2H_4 metrics.

Figure 5a presents the CO_2 reduction gaseous product distribution and C_2H_4 partial current densities of Cu-Ni-N-AC between -1.0 and -1.2V_{RHE}, showing a similar trend with carbon black-supported Cu yet with deviating magnitudes. It can be seen that cell hydrodynamics begin to alter the distribution at potentials slightly negative than -1.1V_{RHE}, as the C_1/C_2 ratio shifts in favor of methane. Therefore, the comparison made in Figure 5b focuses on potentials more positive than -1.1V_{RHE} where these effects
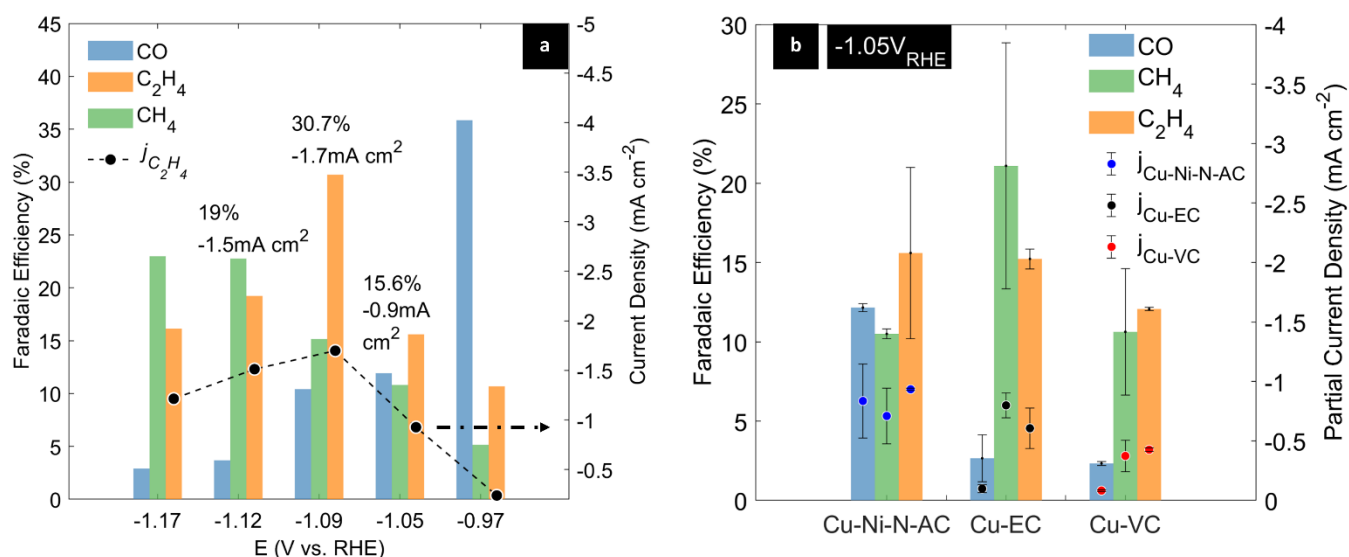

Figure 5 (a) Product Selectivity as a function of potential for Cu-Ni-N-AC and (b) partial current density comparison of Cu-Ni-N-AC, Cu-EC and Cu-VC at -1.05V_{RHE} in 0.1M KHCO$_3$

are negligible. At -1.05V_{RHE}, the CO selectivity decreased from 53.7% on the blank Ni-N-AC to 12.15% on Cu-Ni-N-AC while ECSA-normalized partial current densities increased slightly from -0.64 mA cm_{norm}^{-2} to -0.75 mA cm_{norm}^{-2}. This increase may be attributed to the additional activity of copper towards CO formation in that potential. The partial ethylene current density increased in absolute value from 0.6±0.1 mA cm_{norm}^{-2} on Cu-EC and 0.43 mA cm_{norm}^{-2} on Cu-VC and Cu-AC, respectively, to 0.85±0.01 mA cm_{norm}^{-2} on Cu-Ni-N-AC. According to the data presented in Table S.4, the net consumption of CO at Cu-Ni-N-AC compared to Cu-AC and Ni-N-AC combined was 0.57 µmol cm^{-2} s^{-1}. From equation S.5 (Section S.5.4, ESI), this corresponds with an maximal ethylene partial current density increase of 0.22 mA cm^{-2}, or a CH$_4$ partial current density increase of 0.33 mA cm^{-2}, accordingly. This calculation shows that while the net gain in CH$_4$ matches the requirement, the net gain in C_2H_4 partial current density doubles it, implying that both improved CO_2 reduction and sequential CO reduction to either methane

or ethylene are favored in the case of the bifunctional catalyst. Moreover, the corresponding C_1/C_2 ratio of Cu-Ni-N-AC amounted to 0.67 in average, lower (i.e. promoting ethylene formation) than the value obtained for Cu-EC and within the experimental error for Cu-VC. Compared to the latter, partial current densities of Cu-Ni-N-AC towards ethylene increased 2-fold.

In light of the higher ECSA-normalized CO partial current density of Cu-Ni-N-AC compared to Cu-EC and Cu-AC, one can argue that CO diffuses for the most part away from active sites to the bulk electrolyte, and that the effect of "CO-spillover" or sequential catalysis is still rather limited. A possible explanation for this observation would be the zero solubility of CO under the investigated conditions (<0.2v% in the outlet gas stream, pCO_2 ~1atm), and the fact that bubble nucleation and growth occur rapidly at rough surfaces such as the electrodes in question, in stark contrast to the surfaces studied, for example, by Lum et al[22]. However, and in favor of the sequential catalysis hypothesis, the data presented in the Figure 4a-c, Figure 5a and Table S.4 shows that the partial current densities towards ethylene have been significantly enhanced, even at higher overpotentials where the C_1/C_2 ratio is supposed to be influenced by cell hydrodynamics. Moreover, it became clear that at high overpotentials in 0.1M $KHCO_3$, the intrinsic activity and surface composition of the support begin to negatively influence the catalytic activity of copper nanoparticles supported on Ni-N-EC. Based on our observations and the experimental data, it appears that Cu-Ni alloying, Ni metallic impurities and CO_2 depletion due to excessive CO partial current densities are the major factors behind inferior Cu catalytic activity in the case of Cu-Ni-N-EC.

In the next section, we discuss these challenges, that are inherent to the synthesis and testing of bifunctional Ni-N-C-supported Cu NPs - particularly in a liquid cell configuration - and elaborate on how they could be alleviated.

3.3 Discussion

The reported differences in this study between carbon black supported Cu and Ni-N-AC/EC-based catalysts have multiple origins. First, the ECSA-normalized CO partial current densities of blank Ni-N-EC differs by more than one order of magnitude compared to carbon black supported Cu. The CO_2 consumption at $E < -0.9V_{RHE}$ varies accordingly from 0.1% to 0.7% of the gas feed in the case of the former, accompanied by a theoretical non-linear rise of the local electrode pH and decrease of CO_2 concentration within the hydrodynamic boundary layer. The depletion effect is even more pronounced considering the differences in selectivity between the two catalysts, and the fact that per electron transferred, there are 3 times as much CO_2 molecules consumed to produce CO compared with ethylene. In other words, the CO_2RR limiting practical current density is lower for CO production compared to ethylene production. LSV of Ni-N-EC in Argon-saturated 0.1M $KHCO_3$ showed that the activity of blank Ni-N-EC towards HER increases exponentially at $E < -1.0V_{RHE}$. (Figure 3d). A share of this excessive H_2 evolution in CO_2-saturated 0.1M $KHCO_3$ is a result of the total current exceeding the CO_2RR diffusion limiting current. When the cell is pressurized to 0.30 barg, depletion is slowed down because of an increase in the bulk $CO_{2(aq)}$ concentration from 34.7mM to 52.9mM at 18°C (Section S6, ESI†), leading to lower recorded currents and higher CO_2RR selectivity. This outcome led us to the assumption that Ni-N-EC supported copper nanoparticles might have operated under unfavorable local conditions at high overpotentials. To avoid such likelihood, the total catalyst loading was reduced, but this had little or no effect on the performance the material (Cu-Ni-N-EC-AL, Table S.4, ESI†). In a second approach, striving to remove excess Ni, the Ni-N-EC catalyst was treated with 0.1M nitric acid under reflux (i.e. in addition to the treatments with sulphuric acid mentioned in the experimental section) and before applying the ADP procedure. The measured Ni content of Cu-Ni-N-EC (4.91 wt.%, Table 1) after the washing step dropped to 79% of the initial Ni content of Cu-Ni-N-EC-AL, showing that easily leachable Ni species were still present at the surface, in contrast to the expectation.
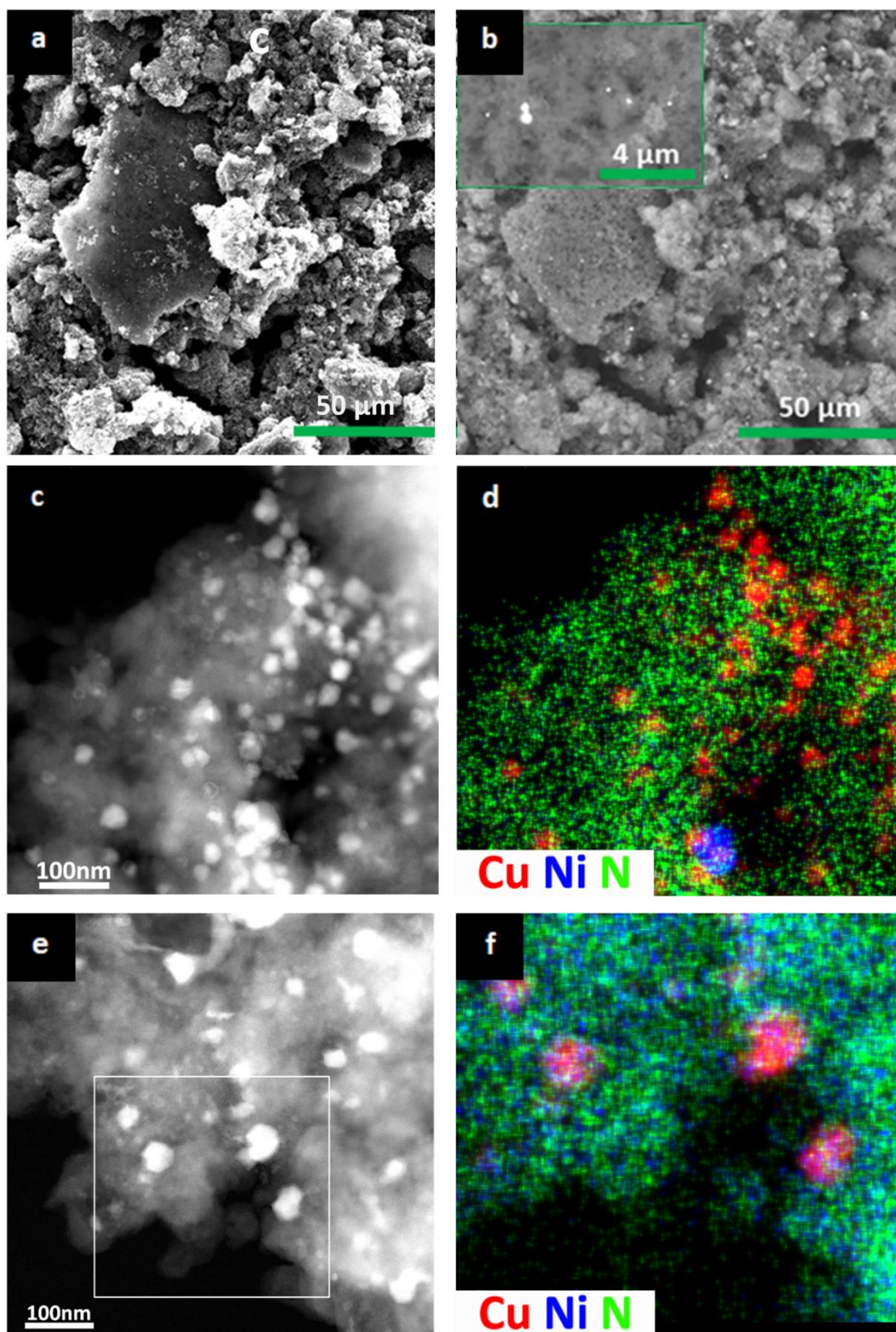
Figure 6 SEM images of blank Ni-N-EC: (a) secondary electrons (SE) image (b) back-scattered electron (BSE) image, showing Ni nanoparticles in the inset, (See also Figure S.13, ESI†) (c, e) HAADF-STEM images and (d, f) the corresponding STEM-EDXS combined elemental maps of the Cu-Ni-N-EC sample after acid-treatment. Individual elemental maps from each element and EDXS spectra are shown in Figure S.14-S.15, ESI†.

Although it was not apparent from low overpotential testing of Ni-N-AC and Ni-N-EC, residual Ni species that were not incorporated into the carbon matrix during the final pyrolysis step of Ni-N-EC/AC synthesis could have in fact contaminated the resulting Cu-decorated catalyst surface. Naturally, during ADP or at high overpotential operation in the electrochemical cell, such surface Ni(OH)$_2$ or NiO species reduce to their metallic form[68], and much in contrast to carbon-coated Ni NPs[69-70], metallic Ni promotes the HER on the one hand[72-73] and may poison the surface of Cu NPs[11, 71] on the other hand. This scenario was confirmed by the aforementioned LSV experiments that showed increased HER under argon saturation, and by SEM observation of the as-synthesized Ni-N-EC catalysts (Figure 6a-b) where back-scattered electron images combined with EDXS analysis showed the presence of Ni nanoparticles at the surface (See also Figure S.13).

Table S.4 shows that the additional acid treatment helped Cu-Ni-N-EC surpass Cu-Ni-N-EC-AL and Ni-N-EC in terms of ECSA-normalized CO partial current density at higher overpotentials. HAADF-STEM and STEM-EDXS data acquired from the Cu-Ni-N-EC catalyst (Figure 6c-d) showed indeed that the surface was largely deprived of Ni NPs. Furthermore, these STEM-EDXS maps (Figure 6e-f) exhibited Cu NPs contiguous to Nitrogen-doped or Ni-N-doped zones – the two are separated by several nanometers at large – and this proximity would have allowed a consideration of "CO spill-over" from Ni-N$_x$ sites to Cu as a possible C$_2$ enhancing mechanism. Despite that, Cu-Ni-N-EC failed to match the results obtained by Cu-Ni-N-AC at -1.05V$_{RHE}$, showing very poor results with an ECSA-normalized ethylene partial current density of -0.14 mA cm$_{norm}^{-2}$ at -1.05V$_{RHE}$. The explanation for its inferior activity compared to Cu-Ni-N-AC is related to the higher recorded CO partial current densities and to the particles' composition, which was further investigated by closely inspecting the XRD and STEM-EDXS data of the samples. Individual STEM-EDXS maps from each element of Cu-Ni-N-EC (Figure S.15, ESI†) revealed distinct Ni signals coinciding with Cu-rich areas, an indication of alloying. We therefore compared the X-ray diffraction patterns of Cu-Ni-N-EC-AL after ADP, with the pattern obtained for the Cu-Ni-N-EC sample. The (111) reflection was shifted 0.07° from 43.37° to 43.3° in case of the Cu-Ni-N-EC sample (Figure S.16), indicating an increase of the cell parameter a from that of a Cu-Ni solid solution (a=3.572Å, 75 at.% Cu) to pure Cu, as predicted from Vegard's law and in

line with literature[74]. STEM-EDXS showed however that some zones still contained alloyed Cu-Ni particles, in addition to other parts containing both pure Cu nanoparticles and individual Ni nanoparticles (Figure S.14, ESI†). These findings explain both the inferior ethylene formation on Cu-Ni-N-EC, due to Cu-Ni alloying, as well as the improved CO activity (compared to the untreated Cu-Ni-N-EC-AL sample), presumably because of partial Ni removal – as confirmed by XRD and ICP-MS.

To conclude, several limitations presented in this section - namely CO_2 depletion and Cu-Ni alloying - strengthen the notion that the bifunctional electrocatalyst concept should be further tested in a different cell configuration, as it is well known that CO_2 or CO reduction in a gas-liquid cell configuration are not limited by gas supply to the electrode, depending of course on the flow rate, potential and loading. With respect to the latter, the Ni metal loading of the support material can be lowered without severe penalty in terms of activity because of the more favorable mass transfer conditions. At the same time, the probability of Cu-Ni alloying will diminish, as was shown in the case of Cu-Ni-N-AC. In addition, an alkaline electrolyte facilitates CO_2 reduction[75] and CO reduction to ethylene[17] and alcohols[76] while it suppresses the HER. We have evidence that Ni-N-C catalysts are highly active towards CO_2RR to CO in 1M KOH at low-moderate overpotentials in such a setup, which means that they can directly reduce gaseous CO_2, but not CO. Because of that, Figure 7 presents two possible gas-liquid cell configurations for probing the bifunctional catalyst in future studies, along with a schematic outline of this work.
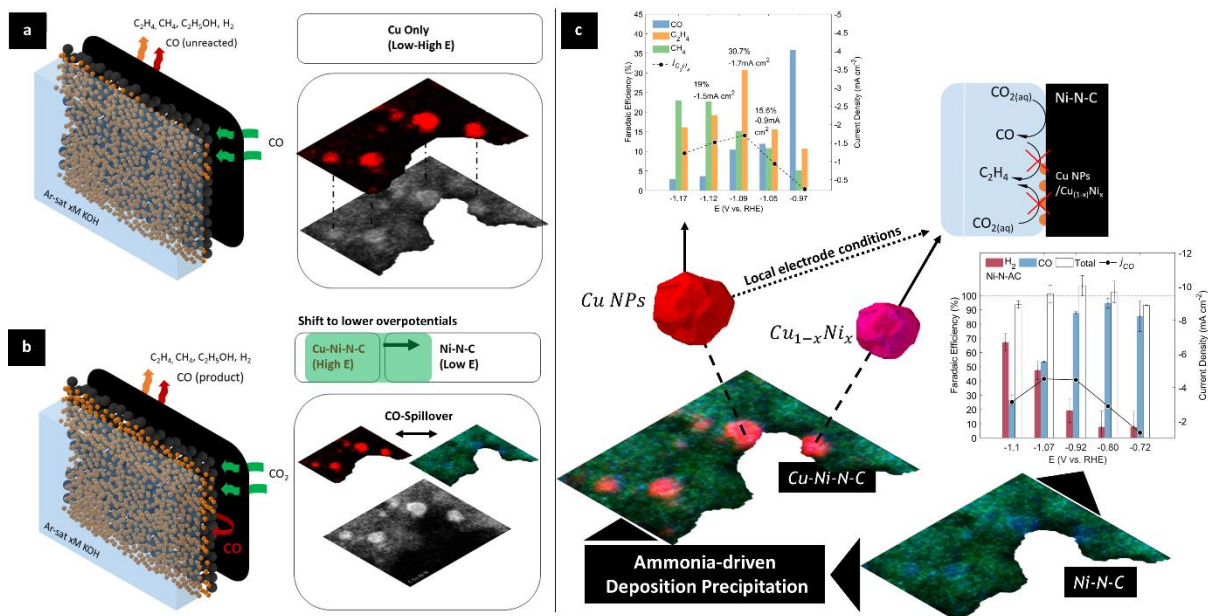
Figure 7 Gas-liquid reaction interfaces for probing the bifunctional catalyst: (a) Flow CO reduction in Ar-saturated xM KOH and (b) Batch/Flow CO_2 reduction in Ar-saturated xM KOH. (c) Schematic outline of this work.

Optimized CO_2 reduction to hydrocarbons or alcohols in a gas-liquid configuration depends of course on myriad parameters – e.g. pressure drop[77], type of membrane, electrolyte composition and CO partial pressure[10], to name but four – and so it goes beyond the scope of this paper. From the catalyst's perspective, the Cu/Ni ratio and both Cu and Ni loading are expected to have a measurable impact on the energy efficiency of the system and this deserves further investigation. These parameters could be varied in future work by adjusting the Ni and nitrogen content of the support or by increasing the Cu loading through mixing, support functionalization or further optimization of catalyst activation steps in the ADP method.

Conclusions

This work has introduced the concept of a bifunctional Ni-N-C-supported Cu electrocatalyst for CO_2 reduction to hydrocarbons. The rationale behind the concept as well as the advantages and challenges it holds, have been extensively discussed. On the practical side, we have demonstrated that copper nanoparticles could be deposited onto carbon black- and nickel-nitrogen-doped carbon by means of an ammonia-driven deposition precipitation (ADP) method. TGA, XRD, H_2-TPR, HAADF-STEM and STEM-EDXS analyses of ion-exchanged, calcined and reduced samples provided information on the different Cu activation steps and on the formation of well-dispersed CuO particles that agglomerate upon thermal reduction to form spherical Cu nanoparticles of 25-50 nm in size. When deposited onto a carbon black support, these particles show activity towards methane and ethylene production at potentials < -1.0V_{RHE} (C_1/C_2 =1.5 at -1.1V_{RHE}), as expected. The C_1/C_2 product ratio (0.5-0.67) at Ni-N-AC-supported Cu nanoparticles is lower compared to carbon black supported Cu, and a 2-fold increase in partial ethylene current density, together with a 10-fold increase of CO production compared to Cu-EC at -1.05V_{RHE} are reported. The enhanced ethylene partial current densities at Cu-Ni-N-AC are in favor of the sequential CO_2 and CO reduction hypothesis, while the higher recorded CO molar flux can be attributed to the higher intrinsic activity of the support. Moreover, we have observed that the following phenomena: formation of metallic Ni NPs after ADP, Cu-Ni alloying and CO_2 depletion caused by the support's intrinsic activity can negatively influence the performance of Cu NPs that are deposited onto a Ni-N-C support – as in the case of Cu-Ni-N-EC. In that respect, we have provided guidelines and methods for the identification of these issues and suggested ways to alleviate them. We take the view that Cu-Ni-N-C electrocatalysts that have passed characterization and liquid cell-configuration tests should be further integrated and evaluated in state-of-the-art gas-liquid reaction interfaces operating under alkaline conditions at low-to-medium overpotentials. Under such conditions, Ni-N-C provides its maximal CO production efficiency and, judging by the results obtained in this study, enhanced partial current densities towards ethylene and CO compared to benchmark carbon black supported Cu could be expected.

Supporting Information

Materials and detailed synthesis procedures, physico-chemical properties of carbon supports (BET and zeta-potentials), additional H_2-TPR and SEM characterization, HAADF-STEM combined with STEM-EDXS and STEM-EELS analysis of Cu-Ni-N-AC, experimental setup and validation thereof, detailed comparisons of electrode performance (potentials, normalized current densities and Faradaic efficiencies), EDXS mappings and spectra of Cu-Ni-N-EC, supporting XRD profiles of Cu-Ni-N-C and comparison of catalytic data with literature.

Acknowledgments

References

1.   Varela, A. S.; Ranjbar Sahraie, N.; Steinberg, J.; Ju, W.; Oh, H.-S.; Strasser, P., Metal-Doped Nitrogenated Carbon as an Efficient Catalyst for Direct Co2 Electroreduction to Co and Hydrocarbons. *Angewandte Chemie International Edition* **2015**, *54*, 10758-10762.
2.   Ju, W.; Bagger, A.; Hao, G.-P.; Varela, A. S.; Sinev, I.; Bon, V.; Roldan Cuenya, B.; Kaskel, S.; Rossmeisl, J.; Strasser, P., Understanding Activity and Selectivity of Metal-Nitrogen-Doped Carbon Catalysts for Electrochemical Reduction of Co2. *Nature Communications* **2017**, *8*, 944.
3.   Ren, W. H.; Tan, X.; Yang, W. F.; Jia, C.; Xu, S. M.; Wang, K. X.; Smith, S. C.; Zhao, C., Isolated Diatomic Ni-Fe Metal-Nitrogen Sites for Synergistic Electroreduction of Co2. *Angewandte Chemie-International Edition* **2019**, *58*, 6972-6976.
4.   Varela, A. S.; Ju, W.; Bagger, A.; Franco, P.; Rossmeisl, J.; Strasser, P., Electrochemical Reduction of Co2 on Metal-Nitrogen-Doped Carbon Catalysts. *ACS Catalysis* **2019**, *9*, 7270-7284.

5.   Zheng, T. T.; Jiang, K.; Ta, N.; Hu, Y. F.; Zeng, J.; Liu, J. Y.; Wang, H. T., Large-Scale and Highly Selective Co2 Electrocatalytic Reduction on Nickel Single-Atom Catalyst. *Joule* **2019,** *3,* 265-278.

6.   Gu, J.; Hsu, C. S.; Bai, L. C.; Chen, H. M.; Hu, X. L., Atomically Dispersed Fe3+ Sites Catalyze Efficient Co2 Electroreduction to Co. *Science* **2019,** *364,* 1091-+.

7.   Yan, C.; Li, H.; Ye, Y.; Wu, H.; Cai, F.; Si, R.; Xiao, J.; Miao, S.; Xie, S.; Yang, F., et al., Coordinatively Unsaturated Nickel–Nitrogen Sites Towards Selective and High-Rate Co2 Electroreduction. *Energy & Environmental Science* **2018,** *11,* 1204-1210.

8.   Möller, T.; Ju, W.; Bagger, A.; Wang, X.; Luo, F.; Ngo Thanh, T.; Varela, A. S.; Rossmeisl, J.; Strasser, P., Efficient Co2 to Co Electrolysis on Solid Ni–N–C Catalysts at Industrial Current Densities. *Energy & Environmental Science* **2019,** *12,* 640-647.

9.   Schouten, K. J. P.; Qin, Z.; Gallent, E. P.; Koper, M. T. M., Two Pathways for the Formation of Ethylene in Co Reduction on Single-Crystal Copper Electrodes. *Journal of the American Chemical Society* **2012,** *134,* 9864-9867.

10.   Li, C. W.; Ciston, J.; Kanan, M. W., Electroreduction of Carbon Monoxide to Liquid Fuel on Oxide-Derived Nanocrystalline Copper. *Nature* **2014,** *508,* 504-507.

11.   Ren, D.; Ang, B. S.-H.; Yeo, B. S., Tuning the Selectivity of Carbon Dioxide Electroreduction toward Ethanol on Oxide-Derived Cuxzn Catalysts. *ACS Catalysis* **2016,** *6,* 8239-8247.

12.   Bagger, A.; Ju, W.; Varela, A. S.; Strasser, P.; Rossmeisl, J., Electrochemical Co2 Reduction: Classifying Cu Facets. *ACS Catalysis* **2019,** *9,* 7894-7899.

13.   Calle-Vallejo, F.; Koper, M. T. M., Theoretical Considerations on the Electroreduction of Co to C2 Species on Cu(100) Electrodes. *Angewandte Chemie International Edition* **2013,** *52,* 7282-7285.

14.   Ledezma-Yanez, I.; Gallent, E. P.; Koper, M. T. M.; Calle-Vallejo, F., Structure-Sensitive Electroreduction of Acetaldehyde to Ethanol on Copper and Its Mechanistic Implications for Co and Co2 Reduction. *Catalysis Today* **2016,** *262,* 90-94.

15.   Garza, A. J.; Bell, A. T.; Head-Gordon, M., Mechanism of Co2 Reduction at Copper Surfaces: Pathways to C2 Products. *ACS Catalysis* **2018,** *8,* 1490-1499.

16.   Schouten, K. J. P.; Pérez Gallent, E.; Koper, M. T. M., The Influence of Ph on the Reduction of Co and to Hydrocarbons on Copper Electrodes. *Journal of Electroanalytical Chemistry* **2014,** *716,* 53-57.

17.   Dinh, C.-T.; Burdyny, T.; Kibria, M. G.; Seifitokaldani, A.; Gabardo, C. M.; de Arquer, F. P. G.; Kiani, A.; Edwards, J. P.; De Luna, P.; Bushuyev, O. S., Co2 Electroreduction to Ethylene Via Hydroxide-Mediated Copper Catalysis at an Abrupt Interface. *Science* **2018,** *360,* 783-787.

18.   Cook, R. L.; MacDuff, R. C.; Sammells, A. F., High Rate Gas Phase Co 2 Reduction to Ethylene and Methane Using Gas Diffusion Electrodes. *Journal of The Electrochemical Society* **1990,** *137,* 607-608.

19.   Ma, S.; Sadakiyo, M.; Luo, R.; Heima, M.; Yamauchi, M.; Kenis, P. J. A., One-Step Electrosynthesis of Ethylene and Ethanol from Co2 in an Alkaline Electrolyzer. *Journal of Power Sources* **2016,** *301,* 219-228.

20.   Dinh, C.-T.; Li, Y. C.; Sargent, E. H., Boosting the Single-Pass Conversion for Renewable Chemical Electrosynthesis. *Joule* **2019,** *3,* 13-15.

21.   Baturina, O.; Lu, Q.; Xu, F.; Purdy, A.; Dyatkin, B.; Sang, X.; Unocic, R.; Brintlinger, T.; Gogotsi, Y., Effect of Nanostructured Carbon Support on Copper Electrocatalytic Activity toward Co2 Electroreduction to Hydrocarbon Fuels. *Catalysis Today* **2017,** *288,* 2-10.

22.   Lum, Y.; Ager, J. W., Sequential Catalysis Controls Selectivity in Electrochemical Co2 Reduction on Cu. *Energy & Environmental Science* **2018,** *11,* 2935-2944.

23.   Huang, J.; Mensi, M.; Oveisi, E.; Mantella, V.; Buonsanti, R., Structural Sensitivities in Bimetallic Catalysts for Electrochemical Co2 Reduction Revealed by Ag–Cu Nanodimers. *Journal of the American Chemical Society* **2019**, *141*, 2490-2499.

24.   Song, Y.; Peng, R.; Hensley, D. K.; Bonnesen, P. V.; Liang, L.; Wu, Z.; Meyer, H. M.; Chi, M.; Ma, C.; Sumpter, B. G., et al., High-Selectivity Electrochemical Conversion of Co2 to Ethanol Using a Copper Nanoparticle/N-Doped Graphene Electrode. *ChemistrySelect* **2016**, *1*, 6055-6061.

25.   Zhang, Y.-J.; Sethuraman, V.; Michalsky, R.; Peterson, A. A., Competition between Co2 Reduction and H2 Evolution on Transition-Metal Electrocatalysts. *ACS Catalysis* **2014**, *4*, 3742-3748.

26.   Li, X.; Bi, W.; Chen, M.; Sun, Y.; Ju, H.; Yan, W.; Zhu, J.; Wu, X.; Chu, W.; Wu, C., et al., Exclusive Ni–N4 Sites Realize near-Unity Co Selectivity for Electrochemical Co2 Reduction. *Journal of the American Chemical Society* **2017**, *139*, 14889-14892.

27.   Xin, Q.; Glisenti, A.; Philippopoulos, C.; Poulakis, E.; Mertens, M.; Nyalosaso, J. L.; Meynen, V.; Cool, P., Comparison between a Water-Based and a Solvent-Based Impregnation Method Towards Dispersed Cuo/Sba-15 Catalysts: Texture, Structure and Catalytic Performance in Automotive Exhaust Gas Abatement. *Catalysts* **2016**, *6*, 164.

28.   Xin, Q.; Papavasiliou, A.; Boukos, N.; Glisenti, A.; Li, J. P. H.; Yang, Y.; Philippopoulos, C. J.; Poulakis, E.; Katsaros, F. K.; Meynen, V., et al., Preparation of Cuo/Sba-15 Catalyst by the Modified Ammonia Driven Deposition Precipitation Method with a High Thermal Stability and an Efficient Automotive Co and Hydrocarbons Conversion. *Applied Catalysis B: Environmental* **2018**, *223*, 103-115.

29.   Gómez-Reynoso, R.; Ramírez, J.; Nares, R.; Luna, R.; Murrieta, F., Characterization and Catalytic Activity of Ni/Sba-15, Synthesized by Deposition–Precipitation. *Catalysis today* **2005**, *107*, 926-932.

30.   de Jong, K. P., *Synthesis of Solid Catalysts*; John Wiley & Sons, 2009.

31.   van der Lee, M. K.; van Dillen, J.; Bitter, J. H.; de Jong, K. P., Deposition Precipitation for the Preparation of Carbon Nanofiber Supported Nickel Catalysts. *Journal of the American Chemical Society* **2005**, *127*, 13573-13582.

32.   Reske, R.; Mistry, H.; Behafarid, F.; Roldan Cuenya, B.; Strasser, P., Particle Size Effects in the Catalytic Electroreduction of Co2 on Cu Nanoparticles. *Journal of the American Chemical Society* **2014**, *136*, 6978-6986.

33.   Baturina, O. A.; Lu, Q.; Padilla, M. A.; Xin, L.; Li, W.; Serov, A.; Artyushkova, K.; Atanassov, P.; Xu, F.; Epshteyn, A., et al., Co2 Electroreduction to Hydrocarbons on Carbon-Supported Cu Nanoparticles. *ACS Catalysis* **2014**, *4*, 3682-3695.

34.   Daems, N.; Sheng, X.; Alvarez-Gallego, Y.; Vankelecom, I. F. J.; Pescarmona, P. P., Iron-Containing N-Doped Carbon Electrocatalysts for the Cogeneration of Hydroxylamine and Electricity in a H2–No Fuel Cell. *Green Chemistry* **2016**, *18*, 1547-1559.

35.   Daems, N.; Wouters, J.; Van Goethem, C.; Baert, K.; Poleunis, C.; Delcorte, A.; Hubin, A.; Vankelecom, I. F. J.; Pescarmona, P. P., Selective Reduction of Nitrobenzene to Aniline over Electrocatalysts Based on Nitrogen-Doped Carbons Containing Non-Noble Metals. *Applied Catalysis B: Environmental* **2018**, *226*, 509-522.

36.   Schlossmacher, P.; Klenov, D. O.; Freitag, B.; von Harrach, H. S., Enhanced Detection Sensitivity with a New Windowless Xeds System for Aem Based on Silicon Drift Detector Technology. *Microscopy Today* **2010**, *18*, 14-20.

37.   Trouillet, L.; Toupance, T.; Villain, F.; Louis, C., In Situ Characterization of the Coordination Sphere of Cuii Complexes Supported on Silica During the Preparation of Cu/Sio2 Catalysts by Cation Exchange. *Physical Chemistry Chemical Physics* **2000**, *2*, 2005-2014.

38.   Shimokawabe, M.; Takezawa, N.; Kobayashi, H., Characterization of Copper-Silica Catalysts Prepared by Ion Exchange. *Applied Catalysis* **1982**, *2*, 379-387.

39.   Lee, K. T.; Ji, X.; Rault, M.; Nazar, L. F., Simple Synthesis of Graphitic Ordered Mesoporous Carbon Materials by a Solid-State Method Using Metal Phthalocyanines. *Angewandte Chemie International Edition* **2009**, *48*, 5661-5665.

40.   Baturina, O. A.; Aubuchon, S. R.; Wynne, K. J., Thermal Stability in Air of Pt/C Catalysts and Pem Fuel Cell Catalyst Layers. *Chemistry of Materials* **2006**, *18*, 1498-1504.

41.   Pinchuk, O. A.; Aubuchon, S. R.; Marks, C.; Dominey, R.; Dundar, F.; Deniz, O. F.; Ata, A.; Wynne, K. J., Thermally Pretreated 46% Pt/Vulcan Xc72: Characterisation by Tga/Dsc/Tem and Cyclic Voltammetry. *Fuel Cells* **2009**, *9*, 554-561.

42.   Ryu, S.-K.; Lee, W.-K.; Park, S.-J., Thermal Decomposition of Hydrated Copper Nitrate [$ Cu (No_3) _2 {\Cdot} 3h_2o $] on Activated Carbon Fibers. *Carbon letters* **2004**, *5*, 180-185.

43.   Padilla, M.; Baturina, O.; Gordon, J. P.; Artyushkova, K.; Atanassov, P.; Serov, A., Selective Co2 Electroreduction to C2h4 on Porous Cu Films Synthesized by Sacrificial Support Method. *Journal of CO2 Utilization* **2017**, *19*, 137-145.

44.   Bond, G. C.; Namijo, S. N.; Wakeman, J. S., Thermal Analysis of Catalyst Precursors: Part 2. Influence of Support and Metal Precursor on the Reducibility of Copper Catalysts. *Journal of Molecular Catalysis* **1991**, *64*, 305-319.

45.   Van Der Grift, C. J. G.; Wielers, A. F. H.; Mulder, A.; Geus, J. W., The Reduction Behaviour of Silica-Supported Copper Catalysts Prepared by Deposition-Precipitation. *Thermochimica Acta* **1990**, *171*, 95-113.

46.   Van Der Grift, C. J. G.; Mulder, A.; Geus, J. W., Characterization of Silica-Supported Copper Catalysts by Means of Temperature-Programmed Reduction. *Applied Catalysis* **1990**, *60*, 181-192.

47.   van den Berg, R.; Parmentier, T. E.; Elkjær, C. F.; Gommes, C. J.; Sehested, J.; Helveg, S.; de Jongh, P. E.; de Jong, K. P., Support Functionalization to Retard Ostwald Ripening in Copper Methanol Synthesis Catalysts. *ACS Catalysis* **2015**, *5*, 4439-4448.

48.   Marchi, A. J.; Fierro, J. L. G.; Santamaría, J.; Monzón, A., Dehydrogenation of Isopropylic Alcohol on a Cu/Sio2 Catalyst: A Study of the Activity Evolution and Reactivation of the Catalyst. *Applied Catalysis A: General* **1996**, *142*, 375-386.

49.   Chen, L.-F.; Guo, P.-J.; Qiao, M.-H.; Yan, S.-R.; Li, H.-X.; Shen, W.; Xu, H.-L.; Fan, K.-N., Cu/Sio2 Catalysts Prepared by the Ammonia-Evaporation Method: Texture, Structure, and Catalytic Performance in Hydrogenation of Dimethyl Oxalate to Ethylene Glycol. *Journal of Catalysis* **2008**, *257*, 172-180.

50.   Huang, Z.; Cui, F.; Xue, J.; Zuo, J.; Chen, J.; Xia, C., Cu/Sio2 Catalysts Prepared by Hom- and Heterogeneous Deposition–Precipitation Methods: Texture, Structure, and Catalytic Performance in the Hydrogenolysis of Glycerol to 1,2-Propanediol. *Catalysis Today* **2012**, *183*, 42-51.

51.   Zhang, B.; Hui, S.; Zhang, S.; Ji, Y.; Li, W.; Fang, D., Effect of Copper Loading on Texture, Structure and Catalytic Performance of Cu/Sio2 Catalyst for Hydrogenation of Dimethyl Oxalate to Ethylene Glycol. *Journal of Natural Gas Chemistry* **2012**, *21*, 563-570.

52.   Zhou, R.-x.; Yu, T.-m.; Jiang, X.-y.; Chen, F.; Zheng, X.-m., Temperature-Programmed Reduction and Temperature-Programmed Desorption Studies of Cuo/Zro2 Catalysts. *Applied Surface Science* **1999**, *148*, 263-270.

53.   Nanda, J.; Kuruvilla, B. A.; Sarma, D. D., Photoelectron Spectroscopic Study of Cds Nanocrystallites. *Physical Review B* **1999**, *59*, 7473-7479.

54.   Nanda, J.; Sapra, S.; Sarma, D. D.; Chandrasekharan, N.; Hodes, G., Size-Selected Zinc Sulfide Nanocrystallites: Synthesis, Structure, and Optical Studies. *Chemistry of Materials* **2000**, *12*, 1018-1024.

55.   Borchert, H.; Shevchenko, E. V.; Robert, A.; Mekis, I.; Kornowski, A.; Grübel, G.; Weller, H., Determination of Nanocrystal Sizes: A Comparison of Tem, Saxs, and Xrd Studies of Highly Monodisperse Copt3 Particles. *Langmuir* **2005**, *21*, 1931-1936.

56.   Arán-Ais, R. M.; Gao, D.; Roldan Cuenya, B., Structure- and Electrolyte-Sensitivity in Co2 Electroreduction. *Accounts of Chemical Research* **2018**, *51*, 2906-2917.

57.   Kim, D.; Kley, C. S.; Li, Y.; Yang, P., Copper Nanoparticle Ensembles for Selective Electroreduction of Co≪Sub≫2≪/Sub≫ to C≪Sub≫2≪/Sub≫– C≪Sub≫3≪/Sub≫ Products. *Proceedings of the National Academy of Sciences* **2017**, *114*, 10560.

58.   Mistry, H.; Behafarid, F.; Reske, R.; Varela, A. S.; Strasser, P.; Roldan Cuenya, B., Tuning Catalytic Selectivity at the Mesoscale Via Interparticle Interactions. *ACS Catalysis* **2016**, *6*, 1075-1080.

59.   Wang, X.; Varela, A. S.; Bergmann, A.; Kühl, S.; Strasser, P., Catalyst Particle Density Controls Hydrocarbon Product Selectivity in Co2 Electroreduction on Cuox. *ChemSusChem* **2017**, *10*, 4642-4649.

60.   Huan, T. N.; Ranjbar, N.; Rousse, G.; Sougrati, M.; Zitolo, A.; Mougel, V.; Jaouen, F.; Fontecave, M., Electrochemical Reduction of Co2 Catalyzed by Fe-N-C Materials: A Structure–Selectivity Study. *ACS Catalysis* **2017**, *7*, 1520-1525.

61.   Clark, E. L.; Resasco, J.; Landers, A.; Lin, J.; Chung, L.-T.; Walton, A.; Hahn, C.; Jaramillo, T. F.; Bell, A. T., Standards and Protocols for Data Acquisition and Reporting for Studies of the Electrochemical Reduction of Carbon Dioxide. *ACS Catalysis* **2018**, *8*, 6560-6570.

62.   Lobaccaro, P.; Singh, M. R.; Clark, E. L.; Kwon, Y.; Bell, A. T.; Ager, J. W., Effects of Temperature and Gas–Liquid Mass Transfer on the Operation of Small Electrochemical Cells for the Quantitative Evaluation of Co2 Reduction Electrocatalysts. *Physical Chemistry Chemical Physics* **2016**, *18*, 26777-26785.

63.   Banerjee, S.; Han, X.; Thoi, V. S., Modulating the Electrode–Electrolyte Interface with Cationic Surfactants in Carbon Dioxide Reduction. *ACS Catalysis* **2019**, 5631-5637.

64.   Singh, M. R.; Kwon, Y.; Lum, Y.; Ager, J. W.; Bell, A. T., Hydrolysis of Electrolyte Cations Enhances the Electrochemical Reduction of Co2 over Ag and Cu. *Journal of the American Chemical Society* **2016**, *138*, 13006-13012.

65.   Resasco, J.; Chen, L. D.; Clark, E.; Tsai, C.; Hahn, C.; Jaramillo, T. F.; Chan, K.; Bell, A. T., Promoter Effects of Alkali Metal Cations on the Electrochemical Reduction of Carbon Dioxide. *Journal of the American Chemical Society* **2017**, *139*, 11277-11287.

66.   Hori, Y.; Murata, A.; Takahashi, R., Formation of Hydrocarbons in the Electrochemical Reduction of Carbon Dioxide at a Copper Electrode in Aqueous Solution. *Journal of the Chemical Society, Faraday Transactions 1: Physical Chemistry in Condensed Phases* **1989**, *85*, 2309-2326.

67.   Kuhl, K. P.; Cave, E. R.; Abram, D. N.; Jaramillo, T. F., New Insights into the Electrochemical Reduction of Carbon Dioxide on Metallic Copper Surfaces. *Energy & Environmental Science* **2012**, *5*, 7050-7059.

68.   Huang, L. F.; Hutchison, M. J.; Santucci, R. J.; Scully, J. R.; Rondinelli, J. M., Improved Electrochemical Phase Diagrams from Theory and Experiment: The Ni–Water System and Its Complex Compounds. *The Journal of Physical Chemistry C* **2017**, *121*, 9782-9789.

69.   Jia, M.; Choi, C.; Wu, T.-S.; Ma, C.; Kang, P.; Tao, H.; Fan, Q.; Hong, S.; Liu, S.; Soo, Y.-L., et al., Carbon-Supported Ni Nanoparticles for Efficient Co2 Electroreduction. *Chemical Science* **2018**, *9*, 8775-8780.

70.   Tan, D.; Cui, C.; Shi, J.; Luo, Z.; Zhang, B.; Tan, X.; Han, B.; Zheng, L.; Zhang, J.; Zhang, J., Nitrogen-Carbon Layer Coated Nickel Nanoparticles for Efficient Electrocatalytic Reduction of Carbon Dioxide. *Nano Research* **2019**, *12*, 1167-1172.

71.   Clark, E. L.; Hahn, C.; Jaramillo, T. F.; Bell, A. T., Electrochemical Co2 Reduction over Compressively Strained Cuag Surface Alloys with Enhanced Multi-Carbon Oxygenate Selectivity. *Journal of the American Chemical Society* **2017**, *139*, 15848-15857.

72.   Hori, Y.; Wakebe, H.; Tsukamoto, T.; Koga, O., Electrocatalytic Process of Co Selectivity in Electrochemical Reduction of Co2 at Metal Electrodes in Aqueous Media. *Electrochimica Acta* **1994**, *39*, 1833-1839.

73.   Jiang, K.; Siahrostami, S.; Zheng, T.; Hu, Y.; Hwang, S.; Stavitski, E.; Peng, Y.; Dynes, J.; Gangisetty, M.; Su, D., et al., Isolated Ni Single Atoms in Graphene Nanosheets for High-Performance Co2 Reduction. *Energy & Environmental Science* **2018**, *11*, 893-903.

74.   Varea, A.; Pellicer, E.; Pané, S.; Nelson, B. J.; Suriñach, S.; Baró, M. D.; Sort, J., Mechanical Properties and Corrosion Behaviour of Nanostructured Cu-Rich Cuni Electrodeposited Films. *Int. J. Electrochem. Sci* **2012**, *7*, 1288-1302.

75.   Dinh, C.-T.; García de Arquer, F. P.; Sinton, D.; Sargent, E. H., High Rate, Selective, and Stable Electroreduction of Co2 to Co in Basic and Neutral Media. *ACS Energy Letters* **2018**, *3*, 2835-2840.

76.   Li, C. W.; Kanan, M. W., Co2 Reduction at Low Overpotential on Cu Electrodes Resulting from the Reduction of Thick Cu2o Films. *Journal of the American Chemical Society* **2012**, *134*, 7231-7234.

77.   Vennekoetter, J.-B.; Sengpiel, R.; Wessling, M., Beyond the Catalyst: How Electrode and Reactor Design Determine the Product Spectrum During Electrochemical Co2 Reduction. *Chemical Engineering Journal* **2019**, *364*, 89-101.

TOC Graphic